The Astrophysical Journal Letters, 902:L16 (7pp), 2020 October 10 https://doi.org/10.3847/2041-8213/abba7a

The MOSDEF Survey: Neon as a Probe of ISM Physical Conditions at High Redshift*

Moon-Seong Jeong[1], Alice E. Shapley[1], Ryan L. Sanders[2,11], Jordan N. Runco[1], Michael W. Topping[1],
Naveen A. Reddy[3], Mariska Kriek[4], Alison L. Coil[5], Bahram Mobasher[3], Brian Siana[3], Irene Shivaei[6,11],
William R. Freeman[3], Mojegan Azadi[7], Sedona H. Price[8], Gene C. K. Leung[5], Tara Fetherolf[3], Laura de Groot[9],
Tom Zick[4], Francesca M. Fornasini[7], and Guillermo Barro[10]
[1] Department of Physics and Astronomy, University of California, Los Angeles, 430 Portola Plaza, Los Angeles, CA 90095, USA; aes@astro.ucla.edu
[2] Department of Physics, University of California, Davis, 1 Shields Avenue, Davis, CA 95616, USA
[3] Department of Physics and Astronomy, University of California, Riverside, 900 University Avenue, Riverside, CA 92521, USA
[4] Astronomy Department, University of California at Berkeley, Berkeley, CA 94720, USA
[5] Center for Astrophysics and Space Sciences, Department of Physics, University of California, San Diego, 9500 Gilman Drive, La Jolla, CA 92093, USA
[6] Steward Observatory, University of Arizona, 933 N Cherry Avenue, Tucson, AZ 85721, USA
[7] Harvard-Smithsonian Center for Astrophysics, 60 Garden Street, Cambridge, MA, 02138, USA
[8] Max-Planck-Institut für Extraterrestrische Physik, Postfach 1312, D-85741 Garching, Germany
[9] Department of Physics, The College of Wooster, 1189 Beall Avenue, Wooster, OH 44691, USA
[10] Department of Physics, University of the Pacific, 3601 Pacific Avenue, Stockton, CA 95211, USA
Received 2020 August 20; revised 2020 September 21; accepted 2020 September 21; published 2020 October 8

Abstract

We present results on the properties of neon emission in $z \sim 2$ star-forming galaxies drawn from the MOSFIRE Deep Evolution Field (MOSDEF) survey. Doubly ionized neon ([Ne III]$\lambda3869$) is detected at $\geqslant 3\sigma$ in 61 galaxies, representing ~25% of the MOSDEF sample with Hα, Hβ, and [O III]$\lambda5007$ detections at similar redshifts. We consider the neon emission-line properties of both individual galaxies with [Ne III]$\lambda3869$ detections and composite $z \sim 2$ spectra binned by stellar mass. With no requirement of [Ne III]$\lambda3869$ detection, the latter provide a more representative picture of neon emission-line properties in the MOSDEF sample. The [Ne III]$\lambda3869$/[O II]$\lambda3727$ ratio (Ne3O2) is anticorrelated with stellar mass in $z \sim 2$ galaxies, as expected based on the mass–metallicity relation. It is also positively correlated with the [O III]$\lambda5007$/[O II]$\lambda3727$ ratio (O32), but $z \sim 2$ line ratios are offset toward higher Ne3O2 at fixed O32, compared with both local star-forming galaxies and individual H II regions. Despite the offset toward higher Ne3O2 at fixed O32 at $z \sim 2$, biases in inferred Ne3O2-based metallicity are small. Accordingly, Ne3O2 may serve as an important metallicity indicator deep into the reionization epoch. Analyzing additional rest-optical line ratios including [Ne III]$\lambda3869$/[O III]$\lambda5007$ (Ne3O3) and [O III]$\lambda5007$/Hβ (O3Hβ), we conclude that the nebular emission-line ratios of $z \sim 2$ star-forming galaxies suggest a harder ionizing spectrum (lower stellar metallicity, i.e., Fe/H) at fixed gas-phase oxygen abundance, compared to systems at $z \sim 0$. These new results based on neon lend support to the physical picture painted by oxygen, nitrogen, hydrogen, and sulfur emission of an ionized interstellar medium in high-redshift star-forming galaxies irradiated by chemically young, α-enhanced massive stars.

Unified Astronomy Thesaurus concepts: Galaxy evolution (594); High-redshift galaxies (734); Interstellar medium (847)

1. Introduction

Rest-optical emission-line spectroscopy provides a comprehensive view of the ionized phase of the interstellar medium (ISM) in star-forming galaxies. Key quantities inferred from nebular emission lines include the instantaneous star formation rate (SFR), dust content, gas-phase oxygen abundance, virial and nonvirial kinematics, and physical ISM gas density. These measurements also describe the radiation field exciting interstellar gas, its intensity and spectral shape, and whether its source is primarily massive stars or an active galactic nucleus (AGN). With the advent of sensitive multi-object near-IR spectrographs on 8–10 m class ground-based telescopes, there has been much recent progress assembling rest-optical emission-line measurements for star-forming galaxies during the epoch of peak star formation in the universe ($z \sim 1.5-3.5$). The next frontier consists of extending such measurements into the epoch of reionization with the James Webb Space Telescope (JWST).

Typically, the strongest rest-optical emission features are the lower Balmer lines (Hα and Hβ) and transitions from singly and doubly ionized oxygen ([O II]$\lambda\lambda3726$, 3729, hereafter [O II]$\lambda3727$, and [O III]$\lambda\lambda4959$, 5007). These features, along with those from singly ionized nitrogen ([N II]$\lambda6584$) and sulfur ([S II]$\lambda\lambda6717$, 6731), have been used to infer the nature of the ionized ISM at $z \sim 2$ and the important ways in which its properties are distinct from those at $z \sim 0$ (e.g., Steidel et al. 2014; Shapley et al. 2019). There is emerging consensus based on recent work from the Keck Baryonic Structure Survey (KBSS; Steidel et al. 2014) and MOSFIRE Deep Evolution Field (MOSDEF) survey (Kriek et al. 2015) that the pattern of rest-optical emission lines observed in $z \sim 2$ star-forming galaxies reflects their chemically young stellar populations. Massive stars in such galaxies are enhanced in α-elements (e.g., oxygen) relative to Fe, and, accordingly, the ionizing spectrum is systematically harder in these distant galaxies compared to local galaxies with similar gas-phase chemical

---

* Based on data obtained at the W.M. Keck Observatory, which is operated as a scientific partnership among the California Institute of Technology, the University of California, and the National Aeronautics and Space Administration, and was made possible by the generous financial support of the W.M. Keck Foundation.

[11] Hubble Fellow.

abundances (Steidel et al. 2016; Strom et al. 2017; Shapley et al. 2019).

The [Ne III]λ3869 feature provides another important probe of the ionized ISM. Nagao et al. (2006) proposed the ratio [Ne III]λ3869/[O II]λ3727 (Ne3O2) as an empirical metallicity indicator (see also Pérez-Montero et al. 2007; Shi et al. 2007), due to its monotonic anticorrelation with oxygen abundance. As discussed in Levesque & Richardson (2014), this anticorrelation arises because [Ne III]λ3869/[O II]λ3727, like [O III] λ5007/[O II]λ3727 (O32), reflects the ionization parameter, which is anticorrelated with metallicity. Due to the difference in ionization potential for [Ne III]λ3869 and [O III]λ5007, however, a comparison of Ne3O2 and O32 ratios in galaxies can also provide a window into the spectral shape of the ionizing radiation field (Strom et al. 2017). Ne3O2 has the advantage over O32 that it is insensitive to dust extinction, due to the proximity in wavelength of [Ne III]λ3869 and [O II] λ3727. Also, based on the short wavelengths of its component features, Ne3O2 can be measured from the ground to $z\sim5$ (Shapley et al. 2017) and, with JWST, all the way to $z\sim12$.

[Ne III]λ3869 is typically fainter than the strongest lines from hydrogen, oxygen, nitrogen, and sulfur, and is only typically detected in lower-metallicity, higher-excitation sources. Accordingly, samples of individual high-redshift galaxies with [Ne III] measurements are not representative of the star-forming galaxy population as a whole. Zeimann et al. (2015) used stacked low-resolution near-IR grism spectra from the Hubble Space Telescope (HST) to investigate the typical properties of neon in low-mass (median $10^9\,M_\odot$) $z\sim2$ star-forming galaxies. Here, we use higher-resolution and deeper near-IR spectroscopy from the MOSDEF survey to investigate the properties of both individual $z\sim2$ galaxies with [Ne III] detections, as well as the average neon emission-line properties in our sample as a function of stellar mass (M_*). These observations provide important complementary constraints on the nature of the ionizing spectrum in high-redshift star-forming galaxies, and have implications for inferring gas-phase metallicities at the earliest times. In Section 2, we present our observations and samples. Section 3 contains our main results, while Section 4 contains a discussion of the implications of these results. Throughout, we assume a ΛCDM cosmology with $H_0=70\,\mathrm{km\,s^{-1}\,Mpc^{-1}}$, $\Omega_m=0.3$, and $\Omega_\Lambda=0.7$. In addition to Ne3O2 and O32, defined previously, we adopt the abbreviations Ne3O3 for the line ratio [Ne III]λ3869/[O III] λ5007, and O3Hβ for [O III]λ5007/Hβ.

2. Observations and Samples

2.1. MOSDEF Survey

Our analysis of emission-line ratios at high redshift focuses on a sample of galaxies drawn from the MOSDEF survey (Kriek et al. 2015). MOSDEF is a near-IR spectroscopic survey of ~1500 galaxies at $1.37\leqslant z\leqslant3.80$. These galaxies lie in the well-studied CANDELS fields (AEGIS, COSMOS, GOODS-N, GOODS-S, and UDS) for which there exist ample supplementary multiwavelength data. With MOSDEF, we used the Multi-object Spectrometer for Infrared Exploration (MOSFIRE; McLean et al. 2012) on the Keck I telescope to obtain moderate-resolution ($R\approx3000$–3650) J-, H-, and K-band spectra probing the rest-optical (~3700–7000 Å) for target galaxies. Further details of the survey observations and data reduction are found in Kriek et al. (2015). Here we discuss some of the aspects of MOSDEF that are most relevant to our analysis.

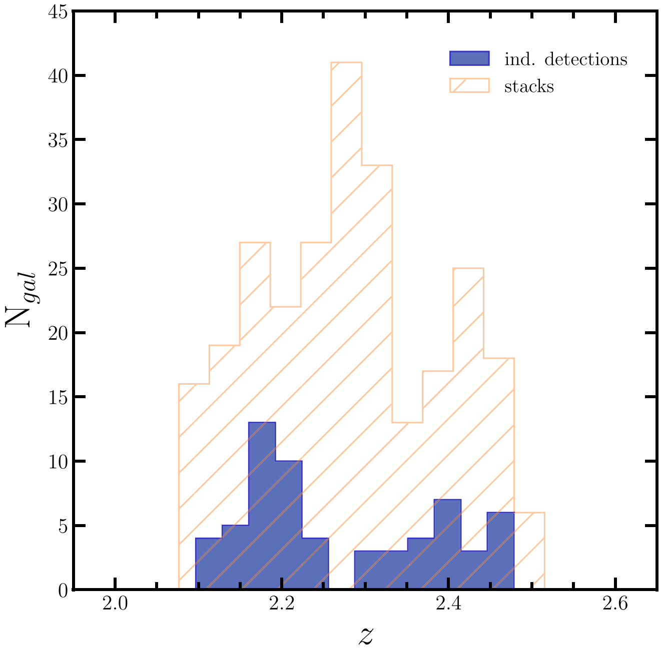

Figure 1. Redshift histograms for $z\sim2$ MOSDEF galaxies with individual [Ne III] detections (solid blue) and those included in the larger sample of MOSDEF composite spectra (hatched orange). The median redshift for the sample of [Ne III] detections is $z_{\mathrm{med,[Ne\,iii]}}=2.223$, while that for the composite sample is $z_{\mathrm{med,comp}}=2.29$.

We studied the rest-optical emission-line fluxes, stellar masses, and dust reddening estimated for $z\sim2$ MOSDEF galaxies. Stellar masses were estimated by fitting emission-line-corrected photometry obtained from the 3D-HST photometric catalogs (Skelton et al. 2014; Momcheva et al. 2016) with FAST, an SED-fitting code (Kriek et al. 2009). The Conroy et al. (2009) flexible stellar population synthesis model, a Chabrier (2003) initial mass function (IMF) and the Calzetti et al. (2000) dust attenuation curve were assumed. We estimated nebular reddening, $E(B-V)_{\mathrm{neb}}$, using the stellar-absorption-corrected Hα/Hβ Balmer decrement for galaxies with Hα and Hβ measurements with signal-to-noise ratio (S/N) greater than or equal to three (S/N $\geqslant3$). We assumed an intrinsic Hα/Hβ emission-line ratio of 2.86 and the Cardelli et al. (1989) extinction law for our calculations.

MOSDEF galaxies were targeted in three redshift bins—$1.37\leqslant z\leqslant1.70$, $2.09\leqslant z\leqslant2.61$, and $2.95\leqslant z\leqslant3.80$—to ensure coverage of bright rest-frame optical emission lines within windows of atmospheric transmission (Kriek et al. 2015). Here we select star-forming galaxies in the $2.09\leqslant z\leqslant2.61$ range with robust detection (S/N $\geqslant3$) in the nebular emission lines of interest: [O II]λ3727, [Ne III] λ3869, Hβ, [O III]λ5007, and Hα. We selected this redshift bin because all of the emission lines of interest fall into the J, H, and K bands, which are covered by the MOSDEF survey. We also excluded AGNs flagged on the basis of X-ray emission, Spitzer/IRAC colors, or [N II]/Hα ratios $\geqslant0.5$ (Coil et al. 2015; Azadi et al. 2017).

Among the 547 star-forming MOSDEF galaxies with a measured redshift at $2.09\leqslant z\leqslant2.61$, only 61 satisfy the requirements for inclusion in the neon detection sample. The redshift distribution of individual [Ne III] detections is shown in Figure 1. The median stellar mass and dust-corrected Hα SFR

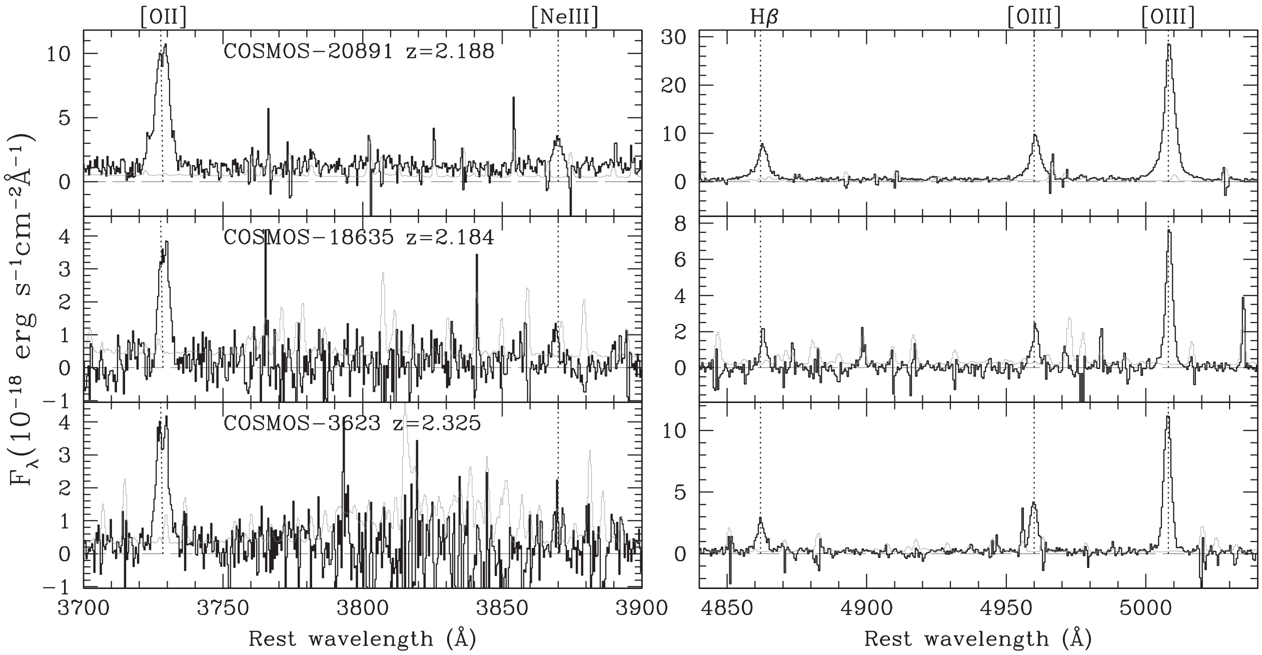

Figure 2. Flux-calibrated *J*-band (left) and *H*-band (right) spectra for three examples from our sample of 61 galaxies with individual [Ne III] detections, demonstrating the range of [Ne III] S/N in the sample. Key nebular emission lines are labeled. *J* band covers [O II] and [Ne III], while *H* band covers Hβ and [O III]. From top to bottom, we show COSMOS-20891, with [Ne III] S/N $\sim$ 12.5 (the highest [Ne III] S/N in the sample); COSMOS-18635, with the median [Ne III] S/N $\sim$ 4; and COSMOS-3623, at the threshold of [Ne III] detection (S/N $\sim$ 3).

Table 1
Masses and Emission-line Ratios of $z \sim 2$ MOSDEF Stacks

$\log\left(\frac{M_*}{M_\odot}\right)$[a]	$\log\left(\frac{M_*}{M_\odot}\right)_{\rm med}$[b]	$N_{\rm gal}$[c]	Ne3O2[d]	Ne3O3[d]	O3Hβ[d]	O32[d]
8.23–9.51	9.29	66	$-0.73^{+0.04}_{-0.04}$	$-0.99^{+0.04}_{-0.04}$	$0.63^{+0.02}_{-0.02}$	$0.26^{+0.02}_{-0.02}$
9.52–9.83	9.72	66	$-0.90^{+0.05}_{-0.05}$	$-0.93^{+0.05}_{-0.05}$	$0.53^{+0.02}_{-0.02}$	$0.03^{+0.02}_{-0.02}$
9.84–10.19	9.99	66	$-1.19^{+0.08}_{-0.10}$	$-1.02^{+0.08}_{-0.10}$	$0.39^{+0.02}_{-0.02}$	$-0.17^{+0.02}_{-0.01}$
10.20–11.27	10.43	66	$-1.04^{+0.06}_{-0.07}$	$-0.70^{+0.06}_{-0.07}$	$0.28^{+0.02}_{-0.02}$	$-0.34^{+0.02}_{-0.02}$

Notes.
[a] Range of $\log(M_*/M_\odot)$ of galaxies in a bin.
[b] Median $\log(M_*/M_\odot)$ of galaxies in a bin.
[c] Number of galaxies in a bin.
[d] Dust-corrected emission-line ratios measured from stacked spectra in each bin.

of the galaxies with [Ne III] detections are, respectively, $\log(M_*/M_\odot) = 9.83$ and 26 $M_\odot$ yr^{-1}. In Figure 2, we show examples of *J*- and *H*-band spectra for galaxies with [Ne III] detections. These spectra cover [O II] and [Ne III] in *J*, and Hβ and [O III] in *H*, and demonstrate the range of S/N spanned by the sample of individual [Ne III] detections.

Given that such a small fraction of the $z \sim 2$ MOSDEF sample shows individual [Ne III] detections, we also analyzed the median emission-line ratios of a more representative sample based on composite spectra in four bins of stellar mass. This sample of 264 galaxies within the same redshift range only has the requirement of Hα and Hβ detections, along with excluding AGNs. Composite spectra were constructed as in Sanders et al. (2018), and the mass ranges, median mass, number of galaxies, and measured line ratios of each composite spectrum are listed in Table 1. The redshift distribution of the stacked sample is also shown in Figure 1. Requiring coverage of [Ne III]λ3869 for both individual detections and composite spectra reduces the redshift range to $2.09 \leqslant z \leqslant 2.50$.

2.2. *Local Comparison Samples*

We compare our $z \sim 2.3$ MOSDEF sample to local data sets including archival data from the Sloan Digital Sky Survey (SDSS) DR7 (Abazajian et al. 2009). We obtain stellar masses and emission-line properties for individual SDSS galaxies at $0.04 \leqslant z \leqslant 0.10$ from the Max Planck Institute for Astrophysics-Johns Hopkins University (MPA-JHU) DR7 release of spectrum measurements.[12] We also made use of the stacked SDSS measurements in bins of stellar mass from Andrews & Martini (2013). Finally, as in Sanders et al. (2017), we use a local H II region catalog from Pilyugin & Grebel (2016), supplemented by observations from Croxall et al. (2016) and Toribio San Cipriano et al. (2016), for a total of 1050 H II regions. Out of the ~97,000 SDSS galaxies with 3σ detections of [O II], Hβ, [O III], Hα, and [N II], which fall on the star-forming side of the AGN versus star-forming curve of

---

[12] https://wwwmpa.mpa-garching.mpg.de/SDSS/DR7/

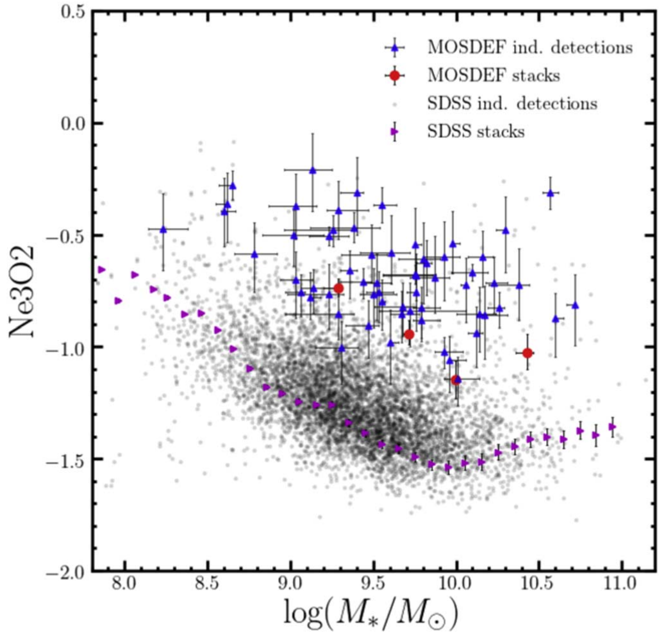

Figure 3. Ne3O2 vs. stellar mass for individual $z \sim 2$ MOSDEF galaxies (blue triangles) and stacked data (red circles) compared with local SDSS galaxies (small gray circles) and stacked data from Andrews & Martini (2013) (purple triangles). In both local and $z \sim 2$ data sets, the stacked Ne3O2 values fall below the median of the individual points at fixed stellar mass, indicating the bias in the [Ne III]-detected samples.

Kauffmann et al. (2003), only 6615 have corresponding detections of the typically weaker [Ne III] feature. On the other hand, [Ne III] is detected in all of the Andrews & Martini (2013) stacks at $\log(M_*/M_\odot) = 8.0 - 11.0$ and in 930 out of 1050 of the H II regions.

3. Results

3.1. Ne3O2 and Stellar Mass

It has been shown that $z \sim 2$ galaxies have systematically higher ionization parameters (in an empirical sense, O32 values) at fixed stellar mass relative to local galaxies (Sanders et al. 2016; Strom et al. 2017). Furthermore, Sanders et al. (2016) and Sanders et al. (2018) find an anticorrelation between O32 and stellar mass in $z \sim 2$ MOSDEF galaxies, as observed in the local universe. This anticorrelation is consistent with the existence of the mass–metallicity relationship at both low and high redshift, given the well-known anticorrelation between ionization parameter and nebular metallicity (Pérez-Montero 2014).

We explored the relationship between Ne3O2 and M_* in the MOSDEF sample, for both individual [Ne III] detections and stacked spectra in bins of M_*. In Figure 3, a clear anticorrelation is observed between Ne3O2 and M_*, although the stacked MOSDEF points fall below the median of the individual [Ne III] detections. A similar difference in Ne3O2 is observed between the individual [Ne III]-detected SDSS points and the stacked spectra from Andrews & Martini (2013). Such offsets are expected given the incompleteness of the [Ne III]-detected samples, and underscores the importance of utilizing the full data set through stacking analysis when the goal is to characterize global emission-line trends and their corresponding physical scaling relationships such as the mass–metallicity relation (Sanders et al. 2018). At fixed stellar mass, $z \sim 2$ MOSDEF stacked spectra are ~0.5 dex higher in Ne3O2 than their local stacked counterparts from Andrews & Martini (2013). We note that the highest-mass (lowest-O32) MOSDEF bin deviates toward elevated Ne3O2 from the monotonic trend present in the three lower-mass bins, which may indicate low-level AGN activity that is not detected on an individual basis.

3.2. Neon Line Ratios as a Probe of ISM Conditions

The line ratio Ne3O2 provides a useful probe of the ionization parameter and, accordingly, the nebular oxygen abundance in star-forming regions (e.g., Nagao et al. 2006; Levesque & Richardson 2014). As demonstrated by Strom et al. (2017), the combination of Ne3O2 and other line ratios such as O32 can also be used to trace quantities such as the hardness of the ionizing spectrum (i.e., the metallicity of the massive stars providing the ionizing radiation field). Due to the higher ionization energy of Ne^+ (40.96 eV) compared with that of O^+ (35.12 eV), harder ionizing spectra at fixed nebular metallicity yield larger Ne3O2 ratios at fixed O32 ratio. In Figure 4, we show the relationship between Ne3O2 and O32 for $z \sim 2$ MOSDEF individual galaxies and stellar-mass stacks, individual SDSS galaxies with [Ne III] detections, and local H II regions. In this space, the SDSS galaxies and H II regions diverge at low O32, likely as the contribution from diffuse ionized gas (DIG) becomes more significant in the integrated galaxy spectra (Sanders et al. 2017; Shapley et al. 2019). Regardless of which local comparison sample is used, the $z \sim 2$ MOSDEF galaxies, including the representative $z \sim 2$ MOSDEF stacks, are offset from local systems toward higher Ne3O2 at fixed O32. Given the wavelength spacing of the individual features in O32, it is necessary to dust correct this feature to infer the intrinsic line ratios in the absence of dust attenuation (left panel of Figure 4). Recent MOSDEF observations suggest that the Cardelli et al. (1989) curve is appropriate for high-redshift nebular dust corrections (Reddy et al. 2020), yet to rule out the possibility that a biased dust correction at high redshift introduces the Ne3O2 offset, we also plot the Ne3O2 versus O32 relation *uncorrected* for dust (right panel). Even without dust correction, the $z \sim 2$ points are offset toward higher Ne3O2 at fixed O32.

As discussed in Shapley et al. (2019), given the ~2 orders of magnitude higher typical SFR surface densities in $z \sim 2$ galaxies compared with their $z \sim 0$ star-forming galaxy counterparts, the integrated spectra from these $z \sim 2$ galaxies likely lack a significant contribution from DIG. Accordingly, the most appropriate local comparison sample for $z \sim 2$ star-forming galaxies is actually individual H II regions, as opposed to SDSS galaxies, the latter of which have significant DIG contribution that leads to systematically different emission-line sequences (Sanders et al. 2017). In order to gain physical insight into the observed Ne3O2 offset at fixed O32, we compare $z \sim 2$ MOSDEF stacked line ratios with local H II regions and photoionization model curves in Figure 5. We consider not only the space of Ne3O2 versus O32, but also Ne3O3 versus O3Hβ, Ne3O3 versus Ne3O2, and O3Hβ versus O32, to untangle the various physical properties in play.

We use the code Cloudy (v17.01; Ferland et al. 2017) with input ionizing spectra from the Binary Population And Spectral Synthesis (BPASS) v2.2.1 models (Eldridge et al. 2017; Stanway & Eldridge 2018). For the BPASS models, we followed the methodology of Topping et al. (2020), varying stellar metallicity over a wide range from extremely subsolar to supersolar, assuming a Chabrier (2003) IMF with a high-mass cutoff of 100 $M_\odot$ and a constant star formation history. We also fixed the

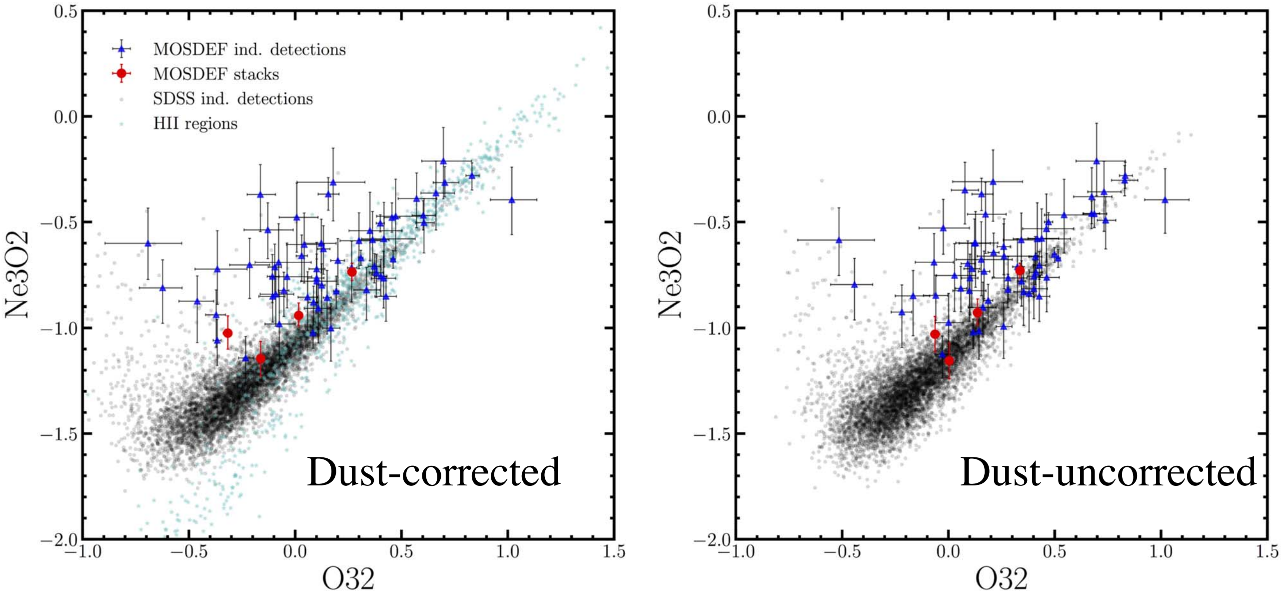

Figure 4. Left: the distribution of dust-corrected Ne3O2 vs. O32 for $z \sim 2$ MOSDEF individual galaxies (blue triangles) and spectral stacks in bins of stellar mass (red circles), along with local SDSS galaxies (small gray circles), and H II regions (small cyan stars). MOSDEF galaxies are offset toward larger Ne3O2 at fixed O32, relative to both SDSS galaxies and H II regions. Right: Ne3O2 vs. O32 for MOSDEF galaxies and stacks, and local SDSS galaxies, with no dust correction applied. H II regions are not included here as only dust-corrected values were tabulated. The same positive offset in Ne3O2 at fixed O32 is observed with no dust correction.

model age to be $t = 10^{8.6}$ yr, although the results are not sensitive to age for $t > 10^{7}$ yr. We furthermore collapsed the model grid to reflect the observed anticorrelation between ionization parameter (U) and oxygen abundance (12 + log(O/H)) at $z \sim 0$ (Pérez-Montero 2014), normalized to pass through the U and 12 + log(O/H) values found for $z \sim 2$ galaxies in Topping et al. (2020): $\log(U) = -1.06 \times (12 + \log(\mathrm{O/H})) + 5.78$.

In all panels of Figure 5 that include neon emission-line ratios (Ne3O2 versus O32, Ne3O3 versus O3Hβ, and Ne3O3 versus Ne3O2), we observe that $z \sim 2$ galaxies are offset from the median $z \sim 0$ H II region distribution toward higher Ne3O2 at fixed O32, higher Ne3O3 at fixed O3Hβ, and higher Ne3O3 at fixed Ne3O2. The distribution of model curves in these diagnostic diagrams suggests that such offsets are indicative of a harder ionizing spectrum (lower stellar metallicity) at fixed nebular metallicity for $z \sim 2$ galaxies. In contrast, changes in ionization parameter at fixed nebular metallicity (Bian et al. 2020) correspond to shifts *along* the distribution of data points. Quantitatively, it is not straightforward to assign a stellar metallicity to the $z \sim 2$ galaxies based on these diagrams, as the model curves do not overlap the full distribution of H II regions and $z \sim 2$ galaxies. However, the negative gradient in stellar metallicity as model curves shift in the direction of the $z \sim 2$ emission-line offset provides a consistent explanation of the differences between high-redshift and local galaxies. We additionally note that $z \sim 2$ galaxies are offset toward higher O3Hβ at fixed O32, which also suggests a lower stellar metallicity at fixed 12 + log(O/H) for high-redshift galaxies.

4. Discussion

The most comprehensive previous analysis of nebular neon emission at $z \sim 2$ was performed by Zeimann et al. (2015). Based on composite HST grism spectra for a sample of 236 galaxies, these authors found a significant enhancement of Ne3O3 relative to local galaxies. Ne3O2 was also $\sim$+0.2 dex more offset at fixed O32 in this sample, relative to our findings. A likely explanation for the smaller enhancements we observe in Ne3O2 and Ne3O3 is contamination of [Ne III] by a blend of He I and Hζ at $\lambda = 3889$Å in low-resolution HST grism spectra (G. Zeimann 2020, private communication), but not in the significantly higher-spectral-resolution MOSDEF stacks, in which He I + Hζ is clearly detected and distinct from [Ne III]. Our results also build on those from Strom et al. (2017), who showed that the average spectrum of 30 $z \sim 2$ KBSS galaxies in the Ne3O2 versus O32 diagram was consistent with a harder ionizing spectrum at fixed nebular metallicity, relative to local systems. We now show a monotonic trend in Ne3O2 versus O32 at $z \sim 2$ in bins of stellar mass over the range 10^{9}–$10^{10}\,M_{\odot}$—but one that is still offset toward enhanced Ne3O2 relative to the local sequence.

The observed enhancements in Ne3O2 and Ne3O3 at $z \sim 2$ relative to local star-forming regions have implications for interpreting other emission-line properties at high redshift. There has been much debate in the literature regarding the observed properties of $z \sim 2$ galaxies in the space of [O III]λ5007/Hβ versus [N II]λ6584/Hα. Possible explanations for the offset between high-redshift and local galaxies include a higher ionization parameter or harder ionizing spectrum, a different N/O abundance pattern, higher electron density, or previously unrecognized AGN activity (e.g., Wright et al. 2010; Kewley et al. 2013; Sanders et al. 2016; Steidel et al. 2016; Kashino et al. 2017). Shapley et al. (2019) used observations of [S II] line ratios in $z \sim 2$ MOSDEF galaxies to show that a harder ionizing spectrum at fixed nebular metallicity provides the best explanation of the sulfur emission-line properties in $z \sim 2$ MOSDEF galaxies. Our results based on neon support the interpretation of a harder ionizing spectrum at fixed nebular metallicity. The shape of the ionizing spectrum is primarily modulated by the Fe abundance of the massive stars providing the ionizing radiation—with harder spectra corresponding to lower Fe abundance—and the nebular metallicity traces the abundance of α-elements such as oxygen. Thus, a harder ionizing spectrum at fixed nebular metallicity is indicative of α-enhancement (i.e., supersolar O/Fe values) in

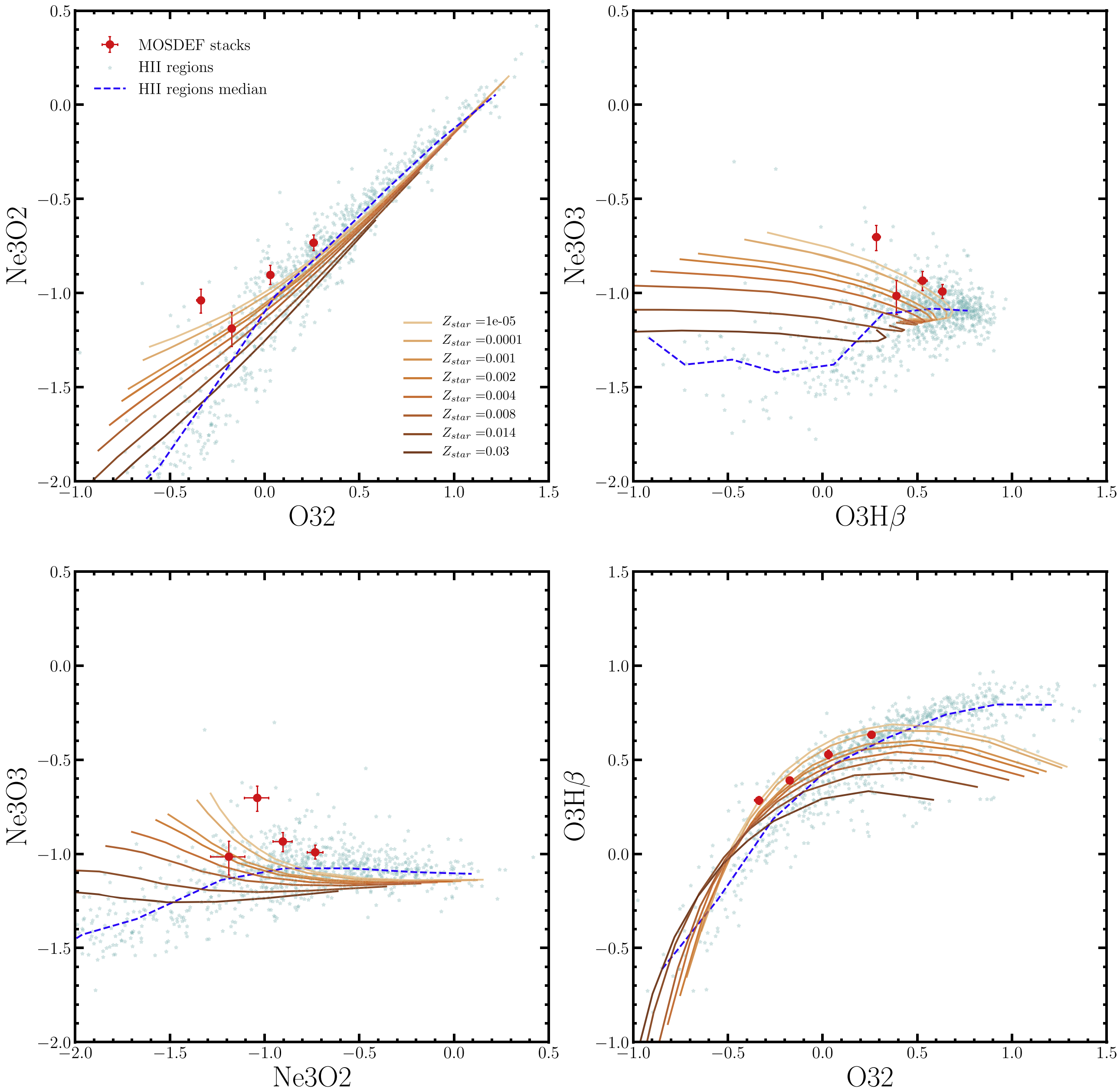

Figure 5. Projections of the dust-corrected emission-line ratio space of [O II]λ3727, [Ne III]λ3869, Hβ, and [O III]λ5007. In each panel, $z \sim 2$ MOSDEF stacks are indicated with red circles and local H II regions with small cyan stars. Blue dashed curves indicate the running median line ratios for the H II regions. Cloudy+BPASS photoionization model curves are overplotted. Each model curve represents a different stellar metallicity (ionizing spectrum), along which ionization parameter (U) and nebular metallicity (12 + log(O/H)) are tied together as described in the text. For each curve of fixed stellar metallicity, U increases and 12 + log(O/H) decreases with increasing O32 or Ne3O2. In the plot of Ne3O3 vs. O3Hβ, ionization parameter increases (nebular metallicity decreases) starting at the upper left of each curve.

the massive stars exciting the ionized gas in star-forming regions at $z \sim 2$ (e.g., Steidel et al. 2016; Sanders et al. 2020). Such abundance patterns are a natural consequence of the young median stellar population ages in $z \sim 2$ star-forming galaxies (Topping et al. 2020). Given the strong evidence for α-enhancement in distant star-forming galaxies, α-enhanced chemical abundance patterns should be considered when modeling their stellar populations and ionized gas.

An important related question is whether Ne3O2 can be used as a robust metallicity indicator at high redshift, given the inferred differences in the ionizing spectrum presented here. At $z \leqslant 3$ there are several other line ratios (e.g., O32, O3Hβ, R23 $\equiv$ log(([O II]λ3727 + [O III]$\lambda\lambda$4959, 5007)/Hβ, N2 $\equiv$ [N II]λ6584/Hα, O3N2 $\equiv$ O3$H\beta$/N2) that can be used for inferring gas-phase oxygen abundance. However, at $z = 3.8-5.0$ from the ground (i.e., K band), and $z \sim 9-12$ (i.e., F290LP filter on JWST/NIRSPEC) from space, Ne3O2 is the only rest-optical line ratio available. We turn to the "local analog" sample of Bian et al. (2018), which serves as an appropriate calibration data set for $z \sim 2$ star-forming galaxies (Sanders et al. 2020), in the absence of a statistical sample of high-redshift objects with direct T_e-based metallicities from which an independent empirical calibration of Ne3O2 to 12 + log(O/H) can be performed. The $z \sim 2$

MOSDEF stacked data are on average 0.08 dex higher in Ne3O2 at fixed O32, relative to the Bian et al. (2018) stacks. The local analog calibration between Ne3O2 and $12 + \log(\mathrm{O/H})$ is $12 + \log(\mathrm{O/H}) = 7.8–0.63 \times \mathrm{Ne3O2}$. Therefore, the average enhancement in Ne3O2 at $z \sim 2$ corresponds to an average underestimate in metallicity of only ~0.05 dex, relative to the local analog sample. Such differences are small compared to the uncertainties in inferred metallicity. Accordingly, we conclude that any biases resulting from estimating metallicity from Ne3O2 alone are not significant at $z \sim 2$. Based on calibration with appropriate lower-redshift analogs, this line ratio may provide extremely important insights into chemical enrichment deep into the reionization era ($z > 9$).

We acknowledge support from NSF AAG grants AST-1312780, 1312547, 1312764, and 1313171; grant AR-13907 from the Space Telescope Science Institute; and grant NNX16AF54G from the NASA ADAP program. We also acknowledge a NASA contract supporting the "WFIRST Extragalactic Potential Observations (EXPO) Science Investigation Team" (15-WFIRST15-0004), administered by GSFC. We thank the 3D-HST collaboration, who provided us with spectroscopic and photometric catalogs used to select MOSDEF targets and derive stellar population parameters. We benefited from useful conversations with Greg Zeimann. We finally wish to extend special thanks to those of Hawaiian ancestry on whose sacred mountain we are privileged to be guests.

ORCID iDs

Alice E. Shapley https://orcid.org/0000-0003-3509-4855
Ryan L. Sanders https://orcid.org/0000-0003-4792-9119
Jordan N. Runco https://orcid.org/0000-0003-4852-8958
Naveen A. Reddy https://orcid.org/0000-0001-9687-4973
Mariska Kriek https://orcid.org/0000-0002-7613-9872
Alison L. Coil https://orcid.org/0000-0002-2583-5894
Brian Siana https://orcid.org/0000-0002-4935-9511
Irene Shivaei https://orcid.org/0000-0003-4702-7561
William R. Freeman https://orcid.org/0000-0003-3559-5270
Mojegan Azadi https://orcid.org/0000-0001-6004-9728
Sedona H. Price https://orcid.org/0000-0002-0108-4176
Gene C. K. Leung https://orcid.org/0000-0002-9393-6507
Tara Fetherolf https://orcid.org/0000-0002-3551-279X
Laura de Groot https://orcid.org/0000-0001-9022-665X
Francesca M. Fornasini https://orcid.org/0000-0002-9286-9963
Guillermo Barro https://orcid.org/0000-0001-6813-875X

References

Abazajian, K. N., Adelman-McCarthy, J. K., Agüeros, M. A., et al. 2009, ApJS, 182, 543
Andrews, B. H., & Martini, P. 2013, ApJ, 765, 140
Azadi, M., Coil, A. L., Aird, J., et al. 2017, ApJ, 835, 27
Bian, F., Kewley, L. J., & Dopita, M. A. 2018, ApJ, 859, 175
Bian, F., Kewley, L. J., Groves, B., & Dopita, M. A. 2020, MNRAS, 493, 580
Calzetti, D., Armus, L., Bohlin, R. C., et al. 2000, ApJ, 533, 682
Cardelli, J. A., Clayton, G. C., & Mathis, J. S. 1989, ApJ, 345, 245
Chabrier, G. 2003, PASP, 115, 763
Coil, A. L., Aird, J., Reddy, N., et al. 2015, ApJ, 801, 35
Conroy, C., Gunn, J. E., & White, M. 2009, ApJ, 699, 486
Croxall, K. V., Pogge, R. W., Berg, D. A., Skillman, E. D., & Moustakas, J. 2016, ApJ, 830, 4
Eldridge, J. J., Stanway, E. R., Xiao, L., et al. 2017, PASA, 34, e058
Ferland, G. J., Chatzikos, M., Guzmán, F., et al. 2017, RMXAA, 53, 385
Kashino, D., Silverman, J. D., Sanders, D., et al. 2017, ApJ, 835, 88
Kauffmann, G., Heckman, T. M., Tremonti, C., et al. 2003, MNRAS, 346, 1055
Kewley, L. J., Dopita, M. A., Leitherer, C., et al. 2013, ApJ, 774, 100
Kriek, M., van Dokkum, P. G., Labbé, I., et al. 2009, ApJ, 700, 221
Kriek, M., Shapley, A. E., Reddy, N. A., et al. 2015, ApJS, 218, 15
Levesque, E. M., & Richardson, M. L. A. 2014, ApJ, 780, 100
McLean, I. S., Steidel, C. C., Epps, H. W., et al. 2012, Proc. SPIE, 8446, 84460J
Momcheva, I. G., Brammer, G. B., van Dokkum, P. G., et al. 2016, ApJS, 225, 27
Nagao, T., Maiolino, R., & Marconi, A. 2006, A&A, 459, 85
Pérez-Montero, E. 2014, MNRAS, 441, 2663
Pérez-Montero, E., Hägele, G. F., Contini, T., & Díaz, Á I. 2007, MNRAS, 381, 125
Pilyugin, L. S., & Grebel, E. K. 2016, MNRAS, 457, 3678
Reddy, N. A., Shapley, A. E., Kriek, M., et al. 2020, arXiv:2009.10085
Sanders, R. L., Shapley, A. E., Zhang, K., & Yan, R. 2017, ApJ, 850, 136
Sanders, R. L., Shapley, A. E., Kriek, M., et al. 2016, ApJL, 825, L23
Sanders, R. L., Shapley, A. E., Kriek, M., et al. 2018, ApJ, 858, 99
Sanders, R. L., Shapley, A. E., Reddy, N. A., et al. 2020, MNRAS, 491, 1427
Shapley, A. E., Sanders, R. L., Reddy, N. A., et al. 2017, ApJL, 846, L30
Shapley, A. E., Sanders, R. L., Shao, P., et al. 2019, ApJL, 881, L35
Shi, F., Zhao, G., & Liang, Y. C. 2007, A&A, 475, 409
Skelton, R. E., Whitaker, K. E., Momcheva, I. G., et al. 2014, ApJS, 214, 24
Stanway, E. R., & Eldridge, J. J. 2018, MNRAS, 479, 75
Steidel, C. C., Strom, A. L., Pettini, M., et al. 2016, ApJ, 826, 159
Steidel, C. C., Rudie, G. C., Strom, A. L., et al. 2014, ApJ, 795, 165
Strom, A. L., Steidel, C. C., Rudie, G. C., et al. 2017, ApJ, 836, 164
Topping, M. W., Shapley, A. E., Reddy, N. A., et al. 2020, MNRAS, 495, 4430
Toribio San Cipriano, L., García-Rojas, J., Esteban, C., Bresolin, F., & Peimbert, M. 2016, MNRAS, 458, 1866
Wright, S. A., Larkin, J. E., Graham, J. R., & Ma, C.-P. 2010, ApJ, 711, 1291
Zeimann, G. R., Ciardullo, R., Gebhardt, H., et al. 2015, ApJ, 798, 29